Available online at www.sciencedirect.com
SCIENCE DIRECT®
C. R. Mecanique 332 (2004) 209–216
COMPTES RENDUS MECANIQUE

Three-dimensional Rayleigh–Bénard instability in a supercritical fluid

Gilbert Accary [a,*], Isabelle Raspo [a], Patrick Bontoux [a], Bernard Zappoli [b]

[a] *MSNM-GP UMR 6181 CNRS, Les Universités d'Aix-Marseille, IMT – La Jetée, Technopôle de Château Gombert, 38, rue Frédéric Joliot Curie, 13451 Marseille cedex 20, France*
[b] *CNES, 18, avenue Edouard Belin, 31401 Toulouse cedex 4, France*

Received 25 November 2003; accepted 13 January 2004

Presented by René Moreau

Abstract

This paper describes the unsteady convective flow of a supercritical fluid in the Rayleigh–Bénard configuration. Two-dimensional earlier studies reported fast temperature equilibrium due to the piston effect and the development of a convective instability when the local Rayleigh number exceeds a critical value. In the present work, a high order 3D finite volume method has been developed and optimized, and to our knowledge, we show for the first time a three-dimensional convective instability in a supercritical fluid. Inspecting the time-evolution of temperature field patterns, we exhibit corner effects and a three-dimensional behavior of the flow. ***To cite this article: G. Accary et al., C. R. Mecanique 332 (2004).***

Résumé

Instabilité tridimensionnelle de Rayleigh–Bénard dans un fluide supercritique. Cet article décrit l'écoulement convectif instationnaire d'un fluide supercritique en configuration de Rayleigh–Bénard. Des études antérieures bidimensionnelles ont montré une homogénéisation rapide de la température par effet piston et le développement d'une instabilité convective lorsque le nombre de Rayleigh local dépasse une valeur critique. Dans le présent travail, une méthode de volumes finis 3D d'ordre élevé a été développée, et à notre connaissance, nous montrons pour la première fois une instabilité convective tridimensionnelle dans un fluide supercritique. En examinant l'évolution temporelle de la structure du champ thermique, nous mettons en évidence des effets de coins et un comportement tridimensionnel de l'écoulement. ***Pour citer cet article : G. Accary et al., C. R. Mecanique 332 (2004).***

Keywords: Fluid mechanics; Supercritical fluid; Rayleigh–Bénard configuration; 3D convective instability; Piston effect

Mots-clés : Mécanique des fluides ; Fluide supercritique ; Configuration de Rayleigh–Bénard ; Instabilité convective 3D ; Effet piston

* Corresponding author.
E-mail address: accary@L3m.univ-mrs.fr (G. Accary).

1631-0721/$ – see front matter
doi:10.1016/j.crme.2004.01.009

Version française abrégée

Les travaux expérimentaux [5,6], théoriques [7,8] et, plus récemment, les études numériques bidimensionnelles [9–12] ont contribué à la compréhension de l'interaction entre la convection naturelle et l'effet piston (EP). Cet effet thermo-acoustique, responsable majeur de l'homogénéisation rapide de la température dans un fluide proche de son point critique, a été observé initialement en microgravité par Nitsche et Straub [1] en 1987 puis prédit théoriquement en 1990 par Boukari et al. [2], Onuki et al. [3], et Zappoli et al. [4].

Dans la continuation des travaux numériques effectués précédemment [9,11], nous étendons la simulation numérique directe aux cas tridimensionnels en considérant dans le présent travail un fluide supercritique dans une cavité cubique en configuration de Rayleigh–Bénard. Nous montrons pour la première fois le développement de structures convectives tridimensionnelles dans un fluide supercritique.

On considère une cavité cubique (Fig. 1) remplie de CO_2 supercritique. Le fluide est initialement au repos, stratifié verticalement en densité et en pression, et en équilibre thermodynamique à une température constante T_i légèrement supérieure à sa température critique T_c. Le modèle mathématique utilisé est celui proposé dans [9]. La simulation numérique commence par l'application d'un faible chauffage ($\Delta T \sim$ quelques mK) sur la paroi inférieure alors que la paroi supérieure est maintenue à la température initiale. Pour cette étude, on considère $T_i - T_c = 1$ K et $\Delta T = 1$ mK. L'écoulement comporte deux phases : le régime dominé par l'EP et le régime convectif.

Les équations régissant l'écoulement sont résolues par une méthode complètement implicite de type volumes finis instationnaire [13] dans l'approximation à faible nombre de Mach [14], sur un maillage structuré non-uniforme. La précision temporelle est du troisième ordre, tandis que la discrétisation spatiale est précise au second ordre [15]. Des méthodes itératives de gradients conjugués et bi-gradients conjugués stabilisées préconditionnées sont utilisées pour la résolution des systèmes linéaires [17]. Le code de calcul est optimisé et opérant à 4.2 Gflops sur le NEC SX-5 de l'IDRIS.

Le chauffage du fluide induit l'apparition d'une fine couche limite thermique le long de la paroi inférieure dans laquelle s'exerce la diffusion. Cette couche limite se dilate fortement et comprime adiabatiquement le reste du fluide, entraînant un chauffage homogène du cœur de la cavité par effet thermo-acoustique. Dans ce régime dominé par l'EP, le champ thermique (Fig. 2(a)) est divisé en trois zones distinctes : deux couches limites thermiques et le cœur de la cavité (Fig. 3).

Tant que l'écoulement n'est pas perturbé par la convection, les épaisseurs des couches limites augmentent à la vitesse de la diffusion thermique. Lorsque le nombre de Rayleigh local basé sur cette épaisseur caractéristique dépasse sa valeur critique, une instabilité convective se développe dans les couches limites [11].

Les Figs. 2(b) à 2(i) montrent l'évolution temporelle de la structure du champ thermique en régime convectif. L'instabilité convective se manifeste sous la forme de panaches thermiques qui se développent dans les deux couches limites. En 2(d) et 2(e), une distribution circulaire des structures est observée sur la paroi supérieure, tandis que, sur la paroi inférieure, on voit apparaître des structures en forme de lames verticales. Dans les Figs. 2(g) à 2(i), ces structures convectives sont plus étalées sur les parois adiabatiques, laissant des zones planes où émergent des panaches thermiques par intermittence. Le transfert convectif du fluide entre les parois horizontales et le cœur de la cavité entraîne une accélération de l'équilibre thermique dans toute la cavité (Fig. 3).

Lorsque l'intensité du chauffage augmente (Fig. 4), l'instabilité convective se développe plus tôt et un plus grand nombre de structures apparaissent avec une distribution spatiale dans le plan (x, y) qui coïncide initialement avec la forme géométrique du problème.

1. Introduction

An experimental observation by Nitsche and Straub [1] in 1987 initially showed a fast thermal equilibrium in the absence of the convection in supercritical fluids. This phenomenon, attributed to a thermoacoustic effect

and termed as the 'piston effect' (PE), was predicted theoretically in 1990 by Boukari et al. [2], Onuki et al. [3], and Zappoli et al. [4]. In the past ten years, most of the attention was devoted to the interaction between the PE and the natural convection. Experimental investigations in the Rayleigh–Bénard configuration (Assenheimer and Steinberg for SF_6 [5], Meyer and Kogan [6] for ^3He) revealed the development of a convective instability near critical conditions. Direct numerical simulations (DNS) based on the fully non-linear 2D Navier–Stokes equations [9–11] and simulations based on simplified hydrodynamic equations [12] confirmed the experimental results and contributed to the understanding of the hydrodynamic behavior of such complex flows, where the thermal diffusivity vanishes and the isothermal compressibility diverges as we approach the critical point.

The continuation of the previous works reported in [9–11] led us to extend the DNS to fully three-dimensional cases, showing for the first time, to our knowledge, 3D convective structures in a supercritical fluid, and allowing future numerical investigations in a more realistic approximation where two-dimensional constraints are no longer imposed on the flow. We used the model proposed in [9], while focusing our efforts on the improvement of the numerical method for the space and time accuracies, for the pressure–velocity coupling algorithm, for the computing vectorization and optimization, and for the linear system solvers.

In the present work, we consider a supercritical fluid in the Rayleigh–Bénard configuration. As in 2D case [10, 11], the flow has two time-phases: the PE-dominated flow and the convection-dominated one. Through the time-evolution of the convective structures, we exhibit the three-dimensional behavior of the flow, and we show the heating intensity effects on the temperature field patterns.

2. Model

The problem under investigation is shown in Fig. 1. A supercritical fluid is enclosed in a cubic shape box (side length $L = 10$ mm), heated from below with no-slip walls and insulated vertical ones, subjected to the earth vertical gravitational field g. Initially, the fluid is at rest, in thermodynamic equilibrium at constant temperature T_i slightly above its critical temperature T_c such that: $T_i = (1 + \varepsilon)T_c$, where ε defines the dimensionless proximity to the critical point ($\varepsilon \ll 1$). Under the effects of its weight, the fluid is stratified in pressure and density, with a mean density equal to its critical value ρ_c. The numerical simulation starts with the application of a progressive weak heating ($\Delta T \sim$ few mK) to the bottom box wall, while maintaining the upper one at its initial temperature T_i.

The governing Navier–Stokes equations are those of a Newtonian, viscous, highly expanding, and heat-conducting van der Waals gas. The choice of van der Waals equation of state is a compromise between its simplicity

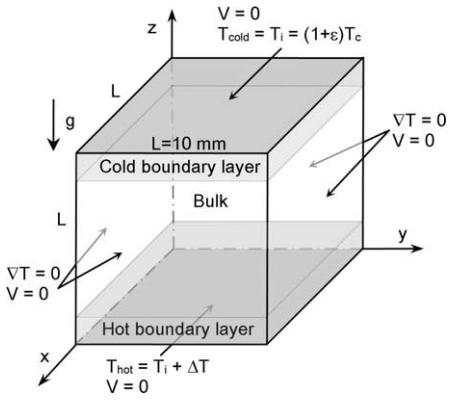

Fig. 1. A supercritical fluid in the Rayleigh–Bénard configuration, with no-slip walls and insulated vertical ones.

Fig. 1. Un fluide supercritique en configuration de Rayleigh–Bénard, avec des conditions de non-glissement sur les parois et des façades verticales adiabatiques.

and its reliable description of the supercritical fluid behavior [9]. A $(1 + \Lambda(T/T_c - 1)^{-1/2})$ law, with $\Lambda = 0.75$, is used to describe the divergence of the thermal conductivity near the critical point, while the heat capacity at constant volume and the molecular viscosity are those of a perfect gas. Using the carbon dioxide intensive thermodynamic variables ($T_c = 304.13$ K, $\rho_c = 468$ Kg/m^3) and transport properties, the equations are made dimensionless as in [9].

3. Numerical method

The governing equations are numerically solved by a fully-implicit finite volume method on staggered mesh [13] in the low Mach number approximation [14], while keeping the gravitational buoyancy force at the leading order in the momentum balance. The space discretization is second order accurate: a centered scheme approaches the diffusion terms, and a high order upwind scheme is used for the convective terms, with Shybrid law incorporation [15] for more accurate solutions when the Peclet number is large. To allow large time scale simulations, the unsteady terms are approached with four time levels, leading to a third order truncation error in time. For each time step, a partial PISO coupling algorithm (velocity prediction, pressure prediction, and velocity correction) is performed [16]. The pressure symmetric equation is solved using the Conjugate Gradient method with Jacobi preconditioning, while the Bi-Conjugate Gradient Stabilized method with the same preconditioner is used for the other non-symmetric transport equations [17]. A structured, non-uniform, power-law mesh is used for an accurate description of the solution in the boundary layers, with 120 computational points in each direction ($\sim$1.7 millions degrees of freedom). With a performance of 4.2 Gflops, the code is vectorized and optimally operating on the IDRIS NEC SX-5 supercomputer. The computational code, adapted to a perfect gas flow, was validated by a comparison with a numerical benchmark for natural convection [18].

4. Results

For this study, we consider $T_i - T_c = 1$ K. To avoid strong initial discontinuities, the bottom wall temperature is linearly increased (with a slope of 1 mK/s) during one second, then, it is held constant at 1 mK for the rest of the simulation.

4.1. Piston effect-dominated flow

The bottom heating induces a wall temperature gradient and the development of a thin thermal boundary layer along the hot wall. A layer in which the diffusion enables the heat transfer and density shows large variations due to the hyper-dilatability of near-critical fluids. This boundary layer expands upward, compressing adiabatically the rest of the fluid, leading to a quick increase of the thermodynamic pressure and to a fast and homogeneous heating of the cavity bulk by thermo-acoustic effects (PE). As the bulk temperature (T_{bulk}) grows, and since the top wall temperature is maintained at its initial value, a cold boundary layer settles near the top wall. Fig. 2(a) shows the temperature field structure at $t = 17.9$ s; in the PE-dominated flow, the temperature field is divided into three distinct zones: two thermal boundary layers along the horizontal walls and the cavity bulk. In Fig. 3, we represent instantaneous mean temperature fields, the (x, y) plan mean temperature is plotted as a function of z-coordinate; the profiles at $t = 1.2$ s and $t = 17.9$ s show clearly the homogenous increase of the bulk temperature induced by the PE.

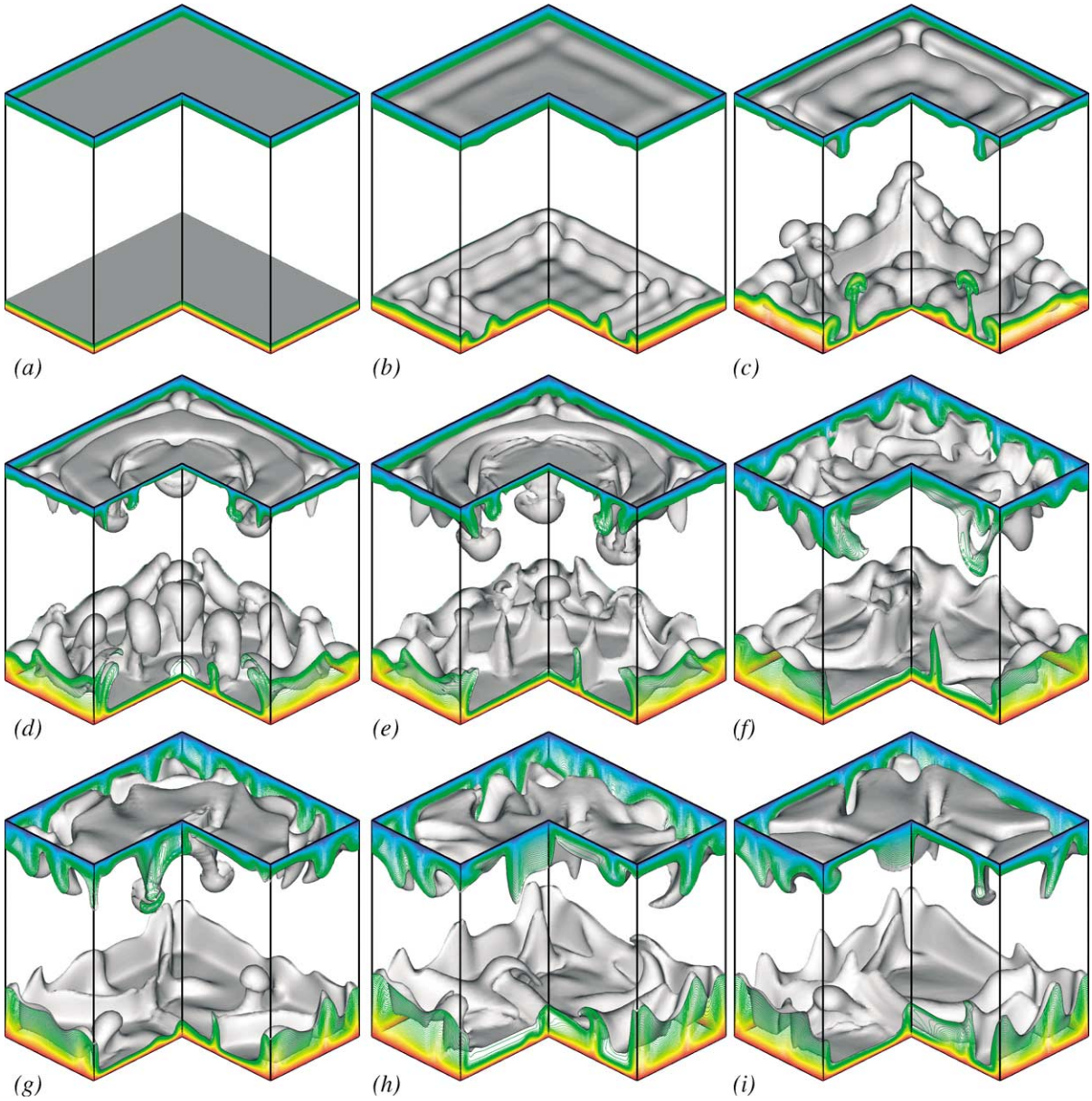

Fig. 2. Instantaneous temperature fields for $\Delta T = 1$ mK, exhibiting the three-dimensionality of the flow. From (a) to (i), $t = 17.9$ s, 22.6 s, 27.4 s, 34.5 s, 36.9 s, 53.6 s, 63.1 s, 72.6 s, 77.4 s, and the shaded isotherms of $(T - T_i)$ in mK are respectively: $(0.44, 0.49)$, $(0.4, 0.6)$, $(0.4, 0.6)$, $(0.4, 0.6)$, $(0.44, 0.6)$, $(0.4, 0.59)$, $(0.37, 0.65)$, $(0.375, 0.625)$, $(0.35, 0.65)$.

Fig. 2. Champs de température instantanés pour $\Delta T = 1$ mK, mettant en évidence le caractère tridimensionnel de l'écoulement. De (a) à (i), $t = 17{,}9$ s, 22,6 s, 27,4 s, 34,5 s, 36,9 s, 53,6 s, 63,1 s, 72,6 s, 77,4 s, et les isothermes ombrées de $(T - T_i)$ en mK sont respectivement : (0,44 ; 0,49), (0,4 ; 0,6), (0,4 ; 0,6), (0,4 ; 0,6), (0,44 ; 0,6), (0,4 ; 0,59), (0,37 ; 0,65), (0,375 ; 0,625), (0,35 ; 0,65).

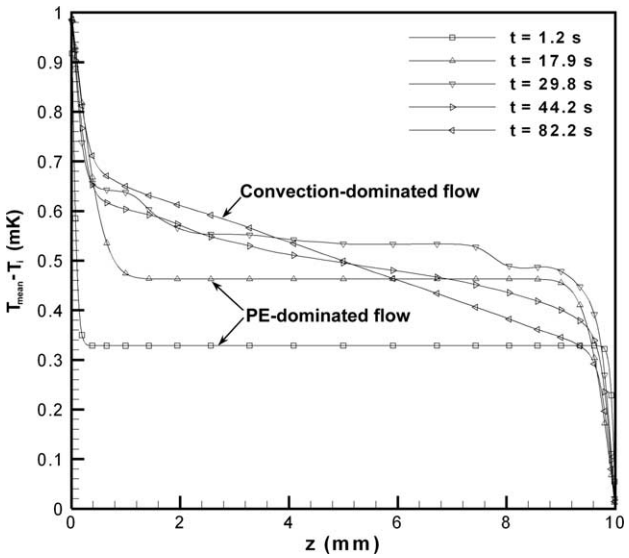

Fig. 3. Instantaneous mean temperature in the (x, y) plan as a function of z-coordinate. In the PE-dominated flow, the bulk temperature is homogeneously increased by the PE; while the convective structures speed up the temperature equilibrium in the convection-dominated flow.

Fig. 3. Profiles instantanés de la température moyenne dans le plan (x, y) en fonction de la coordonnée z. En régime dominé par l'EP, la température du cœur de la cavité est augmentée de manière homogène par EP ; tandis que les structures convectives accélèrent l'équilibre thermique en régime convectif.

4.2. Criterion for convection onset

As long as the flow in the boundary layers is dominated by the diffusion, the thermal boundary layers grow in time at the heat diffusion speed. This thermal expansion is hindered by the density stratification of the fluid, leading to a well-known situation ending with a convective instability when the local Rayleigh number, based on the boundary layer thickness, exceeds a critical value [11]. In the present situation, the Rayleigh number must take into account the stabilizing effect of the adiabatic temperature gradient, as it was shown by Gitterman and Steinberg [7] and, more recently, by Carlès and Ugurtas [8]. The value of the critical Rayleigh number depends on the boundary conditions and is equal to 1100.6 [19] for the present configuration.

4.3. Convection-dominated flow

Figs. 2(b)–(i) show the temperature patterns during significant and duly chosen stages of the convection-dominated flow. Preliminary comparisons with 2D solutions show that the flow is destabilized just about the same time in both cases. Fig. 2(b) illustrates the convection onset: convective plumes rise from both thermal boundary layers; the space distribution of these structures in the (x, y) plan seems to match the squared geometric shape. The thermal plumes are more developed in Fig. 2(c), particularly in the corner regions; 2D sections show very similar patterns to those observed in two-dimensional studies [10,11]. Through Figs. 2(d) and 2(e), the temperature field is subjected to radical changes: on the top wall, a circular distribution of the thermal plumes is observed, while on the bottom wall, some convective structures take vertical fin shapes. In Figs. 2(g) and 2(f), these new shapes are more localized on the bottom wall and spread on the insulated walls leaving flat zones where convective plumes rise, are pinched off, and release thermal balls floating upwards, leaving the horn-like shafts shown in Fig. 2(h). Undergoing changes similar to those at the bottom wall, the temperature patterns on the top wall take vertical fin shapes as shown in Fig. 2(i).

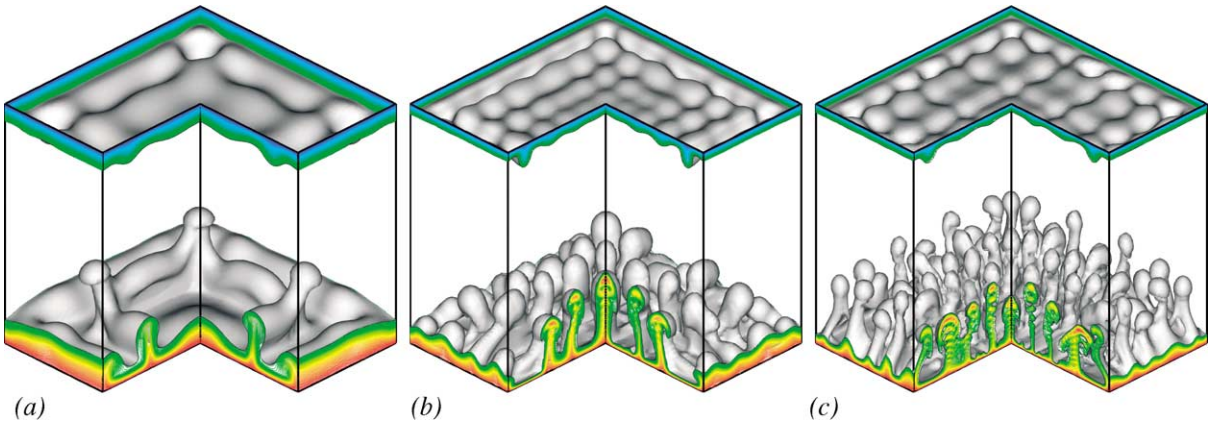

Fig. 4. Heating effects on the instantaneous temperature field. From left to right, $\Delta T = 0.5$ mK, 2.5 mK, and 5 mK; the extraction times are respectively: $t = 45.3$ s, 16.7 s, and 11.4 s; the corresponding shaded isotherms of $(T - T_i)$ in mK are: $(0.2, 0.3)$, $(1.0, 1.5)$, and $(2.2, 3.2)$.

Fig. 4. Effets de l'intensité de chauffage sur le champ instantané de température. De gauche à droite, $\Delta T = 0{,}5$ mK, 2,5 mK et 5 mK ; les instants d'extraction sont respectivement : $t = 45{,}3$ s, 16,7 s et 11,4 s ; les isothermes ombrées de $(T - T_i)$ en mK correspondantes sont : (0,2 ; 0,3), (1,0 ; 1,5) et (2,2 ; 3,2).

The thermal plumes evacuate the hot and cold fluids confined near the bottom and top walls, respectively, to the cavity bulk, causing the collapse of the thermal boundary layers and leading to a convective improvement of the heat transfer between the isothermal walls and the cavity bulk. Consequently, a faster temperature equilibrium in the whole cavity is observed in Fig. 3 ($t = 29.8$ s, 44.2 s, 82.2 s) with the appearance of a bulk slope on the mean temperature profiles.

4.4. Effects of heating intensity

For the same proximity to the critical point and the same mesh, Fig. 4 shows a comparison of the temperature patterns obtained for three values of the temperature drop ΔT: 0.5 mK, 2.5 mK, and 5 mK. A stronger heating increases the number of the convective plumes while reducing their space scales. With an average (x, y) plan resolution of 180 computational points per convective structure, 5 mK heating case can be reasonably modeled. The top wall destabilization is time-delayed in comparison with the bottom one. As the heating increases, the convective instability is released earlier, starting always with an organized space distribution in the (x, y) plan that matches the squared geometric shape. Fig. 4(a) shows some corner effects with the appearance of more developed convective structures near the bottom wall corners.

5. Conclusions

We developed a high order 3D finite volume method for the simulation of the unsteady flow of a van der Waals gas, slightly above its critical point, in the Rayleigh–Bénard configuration. In the PE-dominated flow, we observed a fast bulk temperature equilibrium; as the local Rayleigh number exceeds a critical value, convective instability arises in the form of thermal plumes rising from both hot and cold boundary layers, and the flow becomes convection-dominated. The inspection of instantaneous temperature patterns showed a three-dimensional time-behavior of the flow and important corner effects on the convective structures.

References

[1] K. Nitsche, J. Straub, The critical hump of *Cv* under microgravity, results from D-Spacelab experiment 'Wärmekapazität', in: Proceeding of the 6th European Symp. on Material Sci. under Microgravity Conditions, 1987, p. 109, ESA SP-256.
[2] H. Boukari, J.-N. Schaumeyer, M.-E. Briggs, R.-W. Gammon, Critical speeding up in pure fluids, Phys. Rev. A 41 (1990) 2260.
[3] A. Onuki, H. Hao, R.-A. Ferrel, Fast adiabatic equilibration in a single-component fluid near the liquid–vapor critical point, Phys. Rev. A 41 (1990) 2256.
[4] B. Zappoli, D. Bailly, Y. Garrabos, B. Le Neindre, P. Guenoun, D. Beysens, Anomalous heat transport by the piston effect in supercritical fluids under zero gravity, Phys. Rev. A 41 (1990) 2224.
[5] M. Assenheimer, V. Steinberg, Rayleigh–Bénard convection near gas–liquid critical point, Phys. Rev. Lett. 70 (1993) 3888.
[6] H. Meyer, A.-B. Kogan, Onset of convection in a very compressible fluid: the transient toward steady state, Phys. Rev. E 63 (2002) 056310.
[7] M. Gitterman, V.-A. Steinberg, Criteria for the commencement of convection in a liquid close to the critical point, High Temp. (USSR) 8 (4) (1970) 754.
[8] P. Carlès, B. Ugurtas, The onset of free convection near the liquid–vapour critical point. Part I: Stationary initial state, Physica D 126 (1999) 69.
[9] B. Zappoli, S. Amiroudine, P. Carlès, J. Ouazzani, Thermoacoustic and buoyancy-driven transport in a square side-heated cavity filled with a near-critical fluid, J. Fluid Mech. 316 (1996) 53.
[10] I. Raspo, B. Gilly, S. Amiroudine, P. Bontoux, B. Zappoli, Simulation of convective instabilities inside a supercritical fluid layer under Rayleigh–Bénard configuration, J. Chem. Phys. 96 (1999) 1059.
[11] S. Amiroudine, P. Bontoux, P. Larroudé, B. Gilly, B. Zappoli, Direct numerical simulation of instabilities in a two-dimensional near-critical fluid layer heated from below, J. Fluid Mech. 442 (2001) 119.
[12] A. Furukawa, A. Onuki, Convective heat transport in compressible fluids, Phys. Rev. E 66 (2002) 016302.
[13] S.-V. Patankar, Numerical Heat Transfer and Fluid Flow, Hemisphere, New York, 1980.
[14] S. Paolucci, On the filtering of sound from the Navier–Stokes equations, Rep. SAND 82-8257, December, Sandia National Lab., USA, 1982, p. 52.
[15] Y. Li, M. Rudman, Assessment of higher-order upwind schemes incorporating FCT for convection-dominated problems, Numer. Heat Transfer B 27 (1995) 1.
[16] D.-S. Jang, R. Jetli, S. Acharya, Comparison of the Piso, Simpler, and Simplec algorithms fort he treatment of the pressure–velocity coupling in steady flow problems, Numer. Heat Transfer 10 (1986) 209.
[17] R. Barrett, M. Berry, T.-F. Chan, J. Demmel, J.-M. Donato, J. Dongarra, V. Eijkhout, R. Pozo, C. Romine, H. Van der Vorst, Templates for the Solution of Linear Systems: Building Blocks for Iterative Methods, SIAM, Philadelphia, 1994.
[18] R. Becker, M. Braak, Solution of a stationary benchmark problem for natural convection with large temperature difference, Int. J. Therm. Sci. 41 (2002) 428.
[19] S. Chandrasekar, Hydrodynamic and Hydromagnetic Stability, Clarendon Press, Oxford, 1961.